To appear in the *Journal of Geophysical Research*, 2001.

Resolution analysis of finite fault source inversion using one- and three-dimensional Green's functions 1. Strong motions

Robert W. Graves
URS Corporation, Pasadena, California

David J. Wald
U.S. Geological Survey, Pasadena, California

Abstract

We develop a methodology to perform finite fault source inversions from strong motion data using Green's functions (GFs) calculated for a three-dimensional (3-D) velocity structure. The 3-D GFs are calculated numerically by inserting body forces at each of the strong motion sites and then recording the resulting strains along the target fault surface. Using reciprocity, these GFs can be recombined to represent the ground motion at each site for any (heterogeneous) slip distribution on the fault. The reciprocal formulation significantly reduces the required number of 3-D finite difference computations to at most $3N_S$, where N_S is the number of strong motion sites used in the inversion. Using controlled numerical resolution tests, we have examined the relative importance of accurate GFs for finite fault source inversions which rely on near-source ground motions. These experiments use both 1-D and 3-D GFs in inversions for hypothetical rupture models in order (1) to analyze the ability of the 3-D methodology to resolve trade-offs between complex source phenomena and 3-D path effects, (2) to address the sensitivity of the inversion results to uncertainties in the 3-D velocity structure, and (3) to test the adequacy of the 1-D GF method when propagation effects are known to be three-dimensional. We find that given "data" from a prescribed 3-D Earth structure, the use of well-calibrated 3-D GFs in the inversion provides very good resolution of the assumed slip distribution, thus adequately separating source and 3-D propagation effects. In contrast, using a set of inexact 3-D GFs or a set of hybrid 1-D GFs allows only partial recovery of the slip distribution. These findings suggest that in regions of complex geology the use of well-calibrated 3-D GFs has the potential for increased resolution of the rupture process relative to 1-D GFs. However, realizing this full potential requires that the 3-D velocity model and associated GFs should be carefully validated against the true 3-D Earth structure before performing the inverse problem with actual data.

1. Introduction

Over the last several years the dramatic improvement in computational resources, along with the continued development of efficient numerical algorithms, has allowed elastic wave field simulation techniques to be applied to large-scale three-dimensional (3-D) problems. Some recent studies using 3-D calculations to simulate strong ground motions from earthquakes include the work of *Frankel and Vidale* [1992], *Frankel* [1993], *Olsen and Archuleta* [1996], *Wald and Graves* [1998], *Pitarka et al.* [1998], and *Graves* [1998]. The results of these and other studies demonstrate the importance that variable 3-D subsurface structure can have on the propagation and amplification of seismic waves, particularly in regions containing deep sedimentary basins. These propagation effects include the generation of surface waves at basin margins [e.g., *Frankel and Vidale*, 1992], basin edge amplification [e.g., *Pitarka et al.*, 1998], and focusing type amplification [e.g., *Gao et al.*, 1996; *Hartzell et al.*, 1997].

Along with an increased understanding of 3-D propagation effects, these studies also point out the need for accurate models of the earthquake source and rupture process in order to reliably simulate strong ground motions [e.g., *Graves*, 1998]. Recent, well-recorded earthquakes such as Loma Prieta, Landers, Northridge, and Kobe have provided a wealth of information regarding the spatial and temporal complexity of fault rupture. Typically, source rupture models are derived for these and other earthquakes by direct inversion of strong ground motion records alone [e.g., *Beroza*, 1991; *Cohee and Beroza*, 1994; *Zeng and Anderson*, 1996; *Hartzell et al.*, 1996; *Sekiguchi et al.*, 1996] or by using a combined inversion of strong motion, teleseismic, and geodetic data [e.g.,*Hartzell and Heaton*, 1983; *Wald et al.*, 1991; *Wald and Heaton*, 1994; *Wald et al.*, 1996; *Yoshida et al.*, 1996]. The inversions used in these studies all act to minimize the misfit between a set of model predictions and a set of observed responses. To help assess the adequacy of source inversion methods, several recent studies have also examined the trade-offs between model parameterization and the resolvability of various aspects of the source rupture process. These include analyses of the effects of station coverage [e.g., *Iida*, 1993; *Sarao et al.*, 1998], Green's function accuracy [e.g., *Cohee and Beroza*, 1994], and dynamic rupture properties [e.g., *Guatteri and Spudich.*, 2000].

Primarily because of computational limitations, the Green's functions used in all of the aforementioned inversion analyses have been limited to 1-D (plane-layered) structures. For situations such as the Northridge and Kobe earthquakes where strong lateral velocity variations are known to exist, *Wald et al.* [1996], *Zeng and Anderson* [1996], *Wald* [1996], *Sekiguchi et al.* [1996], and *Hartzell et al.* [1999] used a hybrid set of 1-D rock and 1-D soil Green's functions in their inversion procedures. To first order, this hybrid set of 1-D Green's functions accounts for the gross impedance amplification effects between different site types; however, it cannot account for 3-D propagation effects that can also significantly affect the waveforms and amplitudes of the ground motions.

As more detailed 3-D models of crustal structure are developed [e.g., *Magistrale et al.*, 1998; *Brocher et al.*, 1997] and the use of 3-D elastic wave field simulations becomes more routine, it is natural to consider using 3-D Green's functions in the source inversion procedure [e.g., *Liu and Archuleta*, 1999]. However, before doing this in a routine fashion, several important issues need to be examined. These include assessment of (1) the ability of the 3-D methodology to resolve trade-offs between complex source phenomena and complex 3-D path effects, (2) the resolution potential of the hybrid 1-D Green's function method when propagation effects are known to be three-dimensional, and (3) the sensitivity and accuracy of the inversion results to expected uncertainties in the 3-D velocity structure (e.g., the use of inexact or inadequate 3-D Green's functions).

For example, in the Los Angeles region, even with our current state of knowledge of the 3-D subsurface structure, there are still areas where the structure is not well resolved. This can lead to significant uncertainty in the ground motion response, even for relatively long period (5-10 s) energy [e.g., *Wald and Graves*, 1998]. In a situation such as this, we need to determine if a set of inexact 3-D Green's functions is better or worse than a set of hybrid 1-D Green's functions for recovering the source complexity.

In the sections that follow, we first discuss the calculation of 3-D Green's functions using the principal of reciprocity and present some examples demonstrating the effectiveness of this approach. Next, we step through a series of well-controlled source inversion exercises which are designed to test the sensitivity of the inversion procedure to the trade-offs between the 1-D and 3-D Green's functions. To remove all uncertainties other than the effects of wave propagation in this analysis, we perform the inversions using a set of synthetic data in which all of the rupture parameters are

known. Finally, we discuss the results of the various inversion analyses and the implications that these results have for applying the 3-D inversion methodology to actual ground motion data.

2. Three-Dimensional Reciprocal Green's Functions

A theoretical statement of source-receiver reciprocity for seismic wave fields is given by Betti's relation [e.g., *Aki and Richards*, 1980; *Dahlen and Tromp*, 1998]. This relation states that the locations and orientations of source and observation points can be switched and the exact same elastic response will be observed.

For a double-couple source in elastic media, observations on three orthogonal components are needed to fully describe the motion at an observation point. Reconstructing this response using reciprocity requires three separate computations, each one initiated with a single force located at the desired observation point. The response for the double couple source is then obtained by recording the moment tensor contributions at the desired source location for each of the reciprocal force calculations. For a body force oriented along the x_i component, the moment tensor contributions to this component of displacement are

$$mxx_i = \frac{\partial u_x}{\partial x} , \quad (1a)$$

$$myy_i = \frac{\partial u_y}{\partial y} , \quad (1b)$$

$$mzz_i = \frac{\partial u_z}{\partial z} , \quad (1c)$$

$$mxy_i = \left(\frac{\partial u_y}{\partial x} + \frac{\partial u_x}{\partial y} \right) , \quad (1d)$$

$$mxz_i = \left(\frac{\partial u_z}{\partial x} + \frac{\partial u_x}{\partial z} \right) , \quad (1e)$$

$$myz_i = \left(\frac{\partial u_z}{\partial y} + \frac{\partial u_y}{\partial z} \right) , \quad (1f)$$

where u_x, u_y, and u_z are the computed displacements per unit force in the x, y, and z directions, recorded at the desired source location. These responses are appropriately called reciprocal Green's functions (RGFs) because they represent the propagation effects between two locations for a single force component.

The final displacement response (u_i) is then obtained using a weighted sum of the RGFs for each component:

$$u_i = a_1 \, mxx_i + a_2 \, myy_i + a_3 \, mzz_i + a_4 \, mxy_i + a_5 \, mxz_i + a_6 \, myz_i \, . \quad (2)$$

The coefficients $a_1, ..., a_6$ are computed given the strike, dip, rake, and moment of the desired source orientation [e.g., *Aki and Richards*, 1980]. The advantage of this approach using grid-based techniques such as the finite difference (FD) method is that a large number of potential source locations can be imaged using just a few calculations [e.g., *Graves and Clayton*, 1992].

The numerical implementation of the RGF technique using the 3-D staggered grid finite difference method [e.g., *Graves*, 1996b] is straightforward. However, for observation points located on the surface, care must be taken to ensure that the forces inserted at the free surface in the reciprocal calculations obey the appropriate boundary conditions. We have tested the numerical RGF procedure for a variety of source mechanisms and velocity structures by comparing against results calculated for the forward problem using analytic, frequency wave number [e.g., *Saikia*, 1994], and finite difference methods. In all cases, the RGF procedure produces excellent results.

To demonstrate the applicability of the RGF technique within strongly heterogeneous media, we perform simulations of hypothetical events occurring in the San Fernando basin region of southern California using a single observation point located on the surface near the center of the basin (Figure 1). For these tests, the 3-D velocity structure is taken from *Graves* [1996a]. Cross sections through this model are also shown in Figure 1.

Figure 1

Three point sources are used for the comparison, denoted by e01, e02, and e03 in Figure 1. Table 1 gives the mechanism and depth for each source. Two sets of calculations are performed in this test. The first is a direct forward simulation for each source using the source parameters listed in Table 1. The second set is a reciprocal simulation where body forces are inserted at site s01 and RGFs are determined for the travel path to each source location. The desired response is then obtained by weighting and summing the RGFs. For each source the reciprocal simulation should produce the same waveforms as that obtained with the direct solution.

Table 1

Both sets of simulations are computed using the staggered grid FD method. The grid spacing is 0.1

km, and the minimum shear velocity is 0.5 km/s. The source time function is a 0.5 s cosine bell and the results are low-pass filtered at 1 Hz.

Figure 2 compares the three-component velocity time histories obtained for each of the sources using the RGF and direct solution techniques. For each source mechanism there is excellent agreement between the two solution methods for the entire duration of the waveforms. This comparison demonstrates the accuracy and utility of the RGF approach for complex 3-D velocity models.

The reciprocal simulation consists of only three calculations (one for each body force component) per station, regardless of the number of potential source locations. In this test we retain the RGFs only for three source locations; however, the reciprocal simulation images every grid point in the FD model, enabling a great many RGFs to be calculated with just one simulation.

3. Source Inversion Parameterization

Our primary goal is to investigate the sensitivity of the finite fault inversion procedure to propagation differences between 1-D and 3-D velocity models. In order to remove as much uncertainty from this procedure as possible, we have designed a set of well-controlled numerical inversion experiments in which all of the model parameters are known. Recently, *Guatteri and Spudich* [2000] used a similar systematic approach to investigate the resolution of various dynamic rupture parameters through the inversion of strong motion observations.

The basic procedure we use is (1) to generate a set of synthetic ground motion observations using a forward simulation with a prescribed rupture model, 3-D velocity structure, and distribution of stations, (2) to compute RGFs at each station for a target fault plane using both 1-D and 3-D velocity structures, and (3) to perform least squares inversions of the 3-D synthetic ground motion observations using both the hybrid 1-D and 3-D RGFs and compare the resulting slip distributions with the known starting model.

For the inversion procedure the rupture velocity, risetime, fault location and geometry, and slip direction (rake) are held fixed to the known values. The inversion procedure will solve for the only remaining unknown parameter, which is the slip distribution across the fault plane.

In order to place our analysis in a realistic context, we design our numerical experiments following the source inversion analysis that was performed on the Northridge earthquake by *Wald et al.* [1996]. We use the same fault geometry and distribution of strong motion stations used in the previous analysis (Figure 3), along with existing 3-D velocity models of the San Fernando basin region.

3.1. Source Model

The assumed fault plane is 18 km along strike by 24 km downdip, with a strike of 122°, a dip of 40°, and a depth to the top edge of 5 km. The hypocenter is located 5 km along strike and 20 km downdip from the top center location. Table 2 summarizes the fault plane parameters. For the inversion procedure we use a constant rake of 105°, a constant rupture velocity of 3 km/s, and a uniform slip velocity function given by an isosceles triangle with a 0.6 s duration.

The fault plane is divided into 196 subfaults (14 along strike by 14 downdip) with different weights assigned to each subfault to represent the desired heterogeneous slip distribution. For the prescribed rupture model, we assume a simple slip distribution given by two rectangular slip patches (asperities) as shown in Plate 1. The slip on the shallow asperity is a constant 2 m and the slip on the deep asperity is a constant 1 m, to some degree mimicking the slip recovered for Northridge earthquake [e.g., *Wald et al.*, 1996; *Zeng and Anderson*, 1996]. The region surrounding the asperities has zero slip. The use of a simple block-like pattern of slip to generate the synthetic ground motion observations is useful since it allows us to easily identify the resolution capabilities of the various inversion experiments. With this fault geometry and slip distribution, the simulated event has a moment of about 5.3×10^{18} Nm (M_w 6.45).

3.2. Velocity Models

We use two different 3-D velocity models of the San Fernando basin region in our inversion analysis. The first is from *Graves* [1996a] and the second is the version 1 3-D seismic velocity model from the Southern California Earthquake Center [*Magistrale et al.*, 1998]. Hereinafter we refer to these models as Graves and SCEC V1, respectively.

Both of these models are similar in that they use geologic constraints to model subsurface horizons (e.g., depth to basement). The structural makeup of the models tends to differ where these data are sparse, such as in the San Fernando basin region. To represent the velocity structure of the basin sediments,

the Graves model uses discrete, homogeneous layering which is based on the modeling of ground motion waveforms. The velocity structure of the SCEC V1 model is based on empirical relations that have been calibrated with borehole P wave velocity measurements. This results in a smoother vertical distribution of velocity, generally increasing with depth in the basin. In each model the 3-D basin structures are set into a laterally homogeneous background model. *Wald and Graves* [1998] and *Magistrale et al.* [1998] give more detailed discussions of the various attributes of these two models.

Plate 2 compares shear wave velocity cross sections taken from these models along the three profiles shown in Figure 3. These cross sections indicate that the models are similar in their gross structural composition, but substantial differences exist. In general, the Graves model has a smoother basin geometry, with the structures defined by rather long wavelength features (albeit with sharp boundaries). The SCEC V1 model has much more complexity, both within the basins and along the basin boundaries, and this model exhibits rapid lateral variations in velocity over rather short length scales. The structural differences in the models directly reflect the differences in the geologic surfaces used in defining the models. The Graves model uses only a few surfaces, which are smoothly sampled to represent the basin structures. The SCEC V1 model has undergone significant refinement and evolution from its original form, and thus includes many more surfaces with a higher sampling resolution than those in the Graves model.

On a broad scale these two models provide the most reliable and comprehensive information that is currently available regarding the 3-D velocity structure in the San Fernando basin region. More importantly, the difference between the two models provides a measure of the uncertainty that currently exists in our knowledge of the actual 3-D velocity structure. Differences in the velocity models lead directly to differences in wave propagation effects, which can ultimately result in significant differences in the pattern of predicted ground motion observed during an earthquake [*Wald and Graves*, 1998]. Using these two models in our numerical experiments provides a measure of the sensitivity in the inversion procedure related to the uncertainty in our knowledge of the actual 3-D Earth structure.

As part of the inversion analysis, we also use two 1-D velocity models, one designed for rock sites and the other for basin sites. These 1-D models were derived by first grouping the strong motion stations into rock sites and basin sites based on near-surface geology, and then generating a generic "rock" model and a generic "basin" model for each group. Plate 3 compares the generic rock and basin 1-D shear velocity models against the 1-D vertical profiles taken from the Graves and SCEC V1 3-D models at each of the strong motion sites. Although the 1-D profiles taken from the 3-D models exhibit noticeable variability, the generic 1-D models provide a good representation of the average structure for the two site classes.

Plate 3

3.3. Synthetic Ground Motion Observations

Table 3 lists the 18 strong ground motion sites that are used in the inversion experiments (see also, Figure 3). In general, this station distribution provides very good coverage of the near-source region, especially compared to that available in many other source inversion studies. Using the prescribed rupture model, we generate synthetic ground motions at these 18 sites using a forward simulation procedure for each of the two 3-D velocity models, as well as the site-specific (rock or basin) 1-D velocity models. The ground motions are simulated with the staggered grid FD method using the modeling parameters listed in Table 4.

Table 3

Table 4

Figure 4 compares the horizontal ground velocity waveforms simulated using the prescribed slip model (Plate 1) at each of the strong motion sites for the 3-D and 1-D velocity models. These time histories have been low-pass filtered with a corner at 0.667 Hz.

Figure 4

For many of the stations, the synthetics generated with the different velocity models are quite similar, both in amplitude and waveform. This is particularly true for the first arrivals, which are composed of primarily direct arrivals from the source. At later times, both of the 3-D models predict basin-generated arrivals which are not seen in the 1-D simulations.

Some sites (e.g., jens, nwhp, and rrs) have similar waveforms, but show a timing difference between the different velocity models, and a few sites (e.g., ecc, newh, pacd, pard, and sylm) have noticeable differences in amplitude and/or waveform for at least one horizontal component. In general, the motions at stations to the south and east tend to have more similarity for the different velocity models, whereas the motions at stations to the north and west tend to have less similarity. Since the source and rupture process are identical for all of these simulations, the differences seen in the waveforms of Figure 4 directly reflect the different propagational characteristics of

the velocity models. As will be shown later, the slip model inversion procedure can be quite sensitive to these different wave propagation effects.

3.4. Reciprocal Green's Functions

Using the reciprocal simulation method described earlier, RGFs are calculated at each strong motion station for a number of point source locations covering the target fault plane. To minimize sources of uncertainty in the inversion, the target fault plane is defined to be the same 18 km × 24 km fault plane used in the forward simulations (Table 3). This luxury is not available with real earthquakes where the extent of the fault plane must be inferred from aftershock locations or geodetic constraints, thus potentially adding significant uncertainty to the problem. For each reciprocal simulation the RGFs are saved at a total of 4900 point source locations for each horizontal component. We do not calculate RGFs for the vertical component of motion, as this component is typically down weighted (or not used) in source inversion studies, and hence, does not warrant the additional set of calculations. The exact location of the point sources is fixed by the FD grid, and the average distance between adjacent point source locations is about 300 m.

The RGFs are calculated at the 18 stations for the 3-D SCEC V1, the 3-D Graves, and the 1-D rock and basin velocity models. For the 1-D calculations the rock model is used for six stations (ecc, encr, kagc, pacd, ssus, and svsc), and the basin model is used for the remaining 12 stations (cnpk, jens, newh, nwhp, pard, rrs, rse, sati, shrm, spva, sylm, and vnuy). Over 2.6×10^5 multicomponent point source RGFs are calculated in total. Obviously, computing this number of 3-D Green's functions would be impractical using direct forward (i.e., nonreciprocal) calculations.

The target fault plane is divided into 196 subfaults, each with dimensions of 1.29 km × 1.71 km. The motion for each subfault is obtained by summing the responses of all the point source RGFs which are located within that subfault and then normalizing the response to unit slip. In the summation process, each point source is lagged appropriately in time to account for the propagation of the rupture front across the subfault. Thus all subfaults separately include the effects of rupture propagation and directivity. A detailed description of this modeling procedure is given by *Hartzell and Heaton* [1983].

3.5. Inversion Method

A constrained linear least squares inversion procedure is used to obtain the subfault dislocation weights that give the best fit to the observed velocity waveforms. The inversion is constrained by requiring that the slip is positive everywhere, and smoothing can be applied by minimizing the difference in dislocation values between adjacent subfaults. These constraints have been previously discussed by *Hartzell and Heaton* [1983]. Solving for the amplitude of slip on each subfault, given the strong motion observations and subfault synthetic seismograms, is posed as an overdetermined system of linear equations:

$$\mathbf{A}\mathbf{x} \cong \mathbf{b} \,, \tag{3}$$

where $\mathbf{A}$ is the matrix of subfault synthetics, $\mathbf{x}$ is the solution vector consisting of subfault slip weights, and $\mathbf{b}$ is the data vector containing the observed ground motions. Normalization and damping are included by appending a number of rows to the equations:

$$\begin{pmatrix} \mathbf{C_d^{-1}A} \\ \lambda\,\mathbf{S} \end{pmatrix} \mathbf{x} \cong \begin{pmatrix} \mathbf{C_d^{-1}b} \\ \mathbf{0} \end{pmatrix}. \tag{4}$$

Here $\mathbf{C_d^{-1}}$ is an a priori data covariance matrix which normalizes and weights the data, and $\mathbf{S}$ is a matrix of smoothing constraints which minimize the slip difference between adjacent subfaults ($x_i - x_{i+1} = 0$), both along strike and downdip. The linear weight λ controls the trade-off between satisfying these constraints and fitting the data; in the discussion below we simply refer to λ as the smoothing. For the inversion of the seismic data, each component of motion at individual stations is normalized to the maximum value so that larger-amplitude stations do not dominate the solution.

We use the different sets of hybrid 1-D and 3-D subfault Green's functions to invert the synthetic data shown in Figure 4 to determine the slip distribution on the fault. To concentrate on the source arrivals, we restrict the inversions to include only the first 15 s of the ground motion records. Both the observations and subfault GFs are low-pass filtered with a corner at 0.667 Hz and use a time step of 0.1 s.

We use several goodness of fit measures to facilitate comparisons of the results for the various inversion tests. For the time histories we calculate zero-lag cross correlations for each set of observed and predicted waveforms at each station. These are averaged over all stations and components to obtain a single

correlation coefficient (W_{XC}) for each inversion test. Amplitude variability is measured by calculating the standard error of the misfit in peak velocity between the observed and predicted time histories. The misfit is defined as the ratio of the observed (O_i) and predicted (S_i) peak velocity values for each component at each station, and the standard error is expressed in the natural logarithm domain:

$$\ln(\sigma P_v) = \left\{ \frac{1}{(N-1)} \sum_{i=1}^{N} \left[\ln\left(\frac{O_i}{S_i}\right) - B \right]^2 \right\}^{\frac{1}{2}} , \quad (5)$$

where B is the model bias given by

$$B = \frac{1}{N} \sum_{i=1}^{N} \ln\left(\frac{O_i}{S_i}\right) , \quad (6)$$

and N is the total number of stations and components.

Finally, the resolution of the inverted slip model is measured by calculating the zero-lag, spatial cross correlation between the prescribed slip distribution and the inverted slip distribution:

$$S_{XC} = \frac{\sum_{j=1}^{M} P_j I_j}{\left[\sum_{j=1}^{M} {P_j}^2 \sum_{j=1}^{M} {I_j}^2 \right]^{\frac{1}{2}}} . \quad (7)$$

Here, M is the number of subfaults and P_j and I_j are, respectively, the prescribed and inverted slip amounts on subfault j. Since the slip amounts are always positive, the value of S_{XC} can range from 0 at the poorest correlation to 1 at the best. Obviously, this measure is not available in the case of a real earthquake where the exact slip distribution is unknown. However, for our synthetic examples, this measure allows us to quantitatively assess and compare the resolution of the slip distributions obtained in the various tests.

4. Inversion Results

4.1. Three-Dimensional Data and Well-Calibrated 3-D Green's Functions

The first inversion experiment that we consider uses synthetic observations and RGFs, both calculated from the SCEC V1 3-D velocity model. Since the wave propagation aspects of the observations (**b** vector) are matched exactly by the RGFs (**A** matrix), we expect the least squares inversion to fully recover the prescribed slip distribution. Nonetheless, this experiment is useful in order to (1) test the resolution and accuracy of the discrete RGFs in representing rupture across a finite fault and (2) investigate the sensitivity of smoothing values on both the inverted slip model and the predicted ground motions.

Plate 4 shows inversion results for smoothing values of 0.0 (no smoothing), 0.005, and 0.01. With no smoothing (Plate 4b), the prescribed slip distribution is exactly recovered, thus validating the RGF inversion methodology for finite fault ruptures.

In general, when the GFs are less than exact, smoothing must be applied in the inversion to maintain stability. Obviously, the use of smoothing will blur the sharp edges of the slip distribution, as demonstrated by the inversion results shown in Plates 4c and 4d. Since the RGFs used in this experiment are a perfect match for the observations, the results shown in Plate 4 represent the degree that each smoothing value degrades the slip resolution.

The values of smoothing used here are typical of those used in previous inversion analyses. The exact value to use is subjective; however, the amount of smoothing should not be so great that it significantly degrades the fit between the predicted and observed ground motions in the bandwidth of interest. *Sekiguchi et al.* [2000] provide a detailed discussion regarding the optimal choice of smoothing value. Figure 5 compares the observed ground motions with those predicted from the inverted slip model obtained with a smoothing value of 0.01. The match between the observed and predicted waveforms is excellent. The waveform correlation coefficient is 0.99, and the standard error of peak amplitude misfit is 0.059. This indicates that for periods of $T > 1.5$ s, the predicted ground motions are relatively insensitive to smoothing values of 0.01 or less.

4.2. Three-Dimensional Data and Inexact 3-D Green's Functions

We next consider observed ground motions from the SCEC V1 3-D model and subfault synthetics from the Graves 3-D model. The objective here is to investigate the impact on the inversion results when an inexact (or poorly calibrated) set of 3-D GFs are employed.

Plate 5 displays the slip distributions obtained for this experiment. We show results for two cases: The first is obtained using the raw absolute timing of the

GFs, and the second is obtained by applying station-dependent timing shifts to the GFs. The timing shifts account for first-order timing differences between the GFs and observations. This approach has been used in previous inversion analyses [e.g., *Wald et al.*, 1996], and is particularly useful when the timing of the GFs is poorly calibrated or when absolute timing is unavailable for the data. For both inversion cases, results with smoothing values of 0.0, 0.005, and 0.01 are shown.

The timing corrections are estimated for each station by comparing the observed ground motions with the synthetics obtained from the original inversion performed without timing shifts. Figure 6 displays observed and synthetic motions from inversions with and without timing shifts at three stations where the corrections are most significant (of the order of 1 s). These sites are located along the northern margin of the San Fernando basin where the SCEC V1 model has a very deep wedge of low-velocity sediments that results in a delay of the GF relative to the observations (see Plate 2). Applying the timing corrections noticeably improves the waveform match to the observations.

Figure 7 compares the observed and synthetic motions at all stations for the time-corrected inversion using a smoothing value of 0.01. For most stations the match between the observed and calculated motions is fairly good. The waveform correlation coefficient for this result is 0.78, with a peak amplitude error of 0.337. These measures indicate an improvement over the values of 0.64 and 0.372, respectively, that are obtained when timing corrections are not used.

The effect of applying timing corrections to the GFs also improves the resolution of the slip distribution. We quantify the resolution of the slip distribution by calculating the spatial correlation coefficient of the inverted slip distribution (Plate 5) with the prescribed slip distribution (Plate 1). For a smoothing value of 0.01, the inversion without timing corrections has a slip correlation of 0.57, and the inversion including timing corrections has a slip correlation of 0.79. The primary effect of using the timing corrections is to reduce the spurious slip patches along the outer margins of the fault plane, thus concentrating the slip into more box-like asperities (Plate 5).

While the results for this case show differences compared to the results obtained in the previous section using the exact 3-D GFs, the overall pattern of slip (i.e., two asperities) is essentially recovered. This suggests that although the use of poorly calibrated 3-D GFs will degrade the resolution of the inversion procedure, the main features of the slip distribution can still be recovered as long as the gross propagational aspects of the ground motions are included in the Green's functions.

4.3. Three-Dimensional Data and Hybrid 1-D Green's Functions

In this section we analyze results for a set of inversions that use observations generated from the 3-D velocity models with subfault synthetics derived from the hybrid 1-D GFs. These experiments are designed to give an indication of the sensitivity of the hybrid 1-D GFs to variability and uncertainty in the 3-D velocity structure.

Plate 6 displays the inversion results obtained using the hybrid 1-D GFs with the observed ground motions from the SCEC V1 3-D velocity model. We show results for various smoothing values both with and without timing corrections. Figure 8 compares the observed and synthetic ground motions for the time-corrected inversion using a smoothing value of 0.01. As in the previous example, the addition of timing corrections to the GFs significantly improves the resolution of the slip distribution. Without timing corrections the slip tends to be concentrated into small patches at the shallow and deep edges of the fault. Using the timing corrections, the slip is more accurately partitioned into two block-like asperities. Spatial slip correlations for the inversions without and with timing corrections are 0.68 and 0.75, respectively.

The last case we consider uses the hybrid 1-D GFs with observed ground motions calculated from the Graves 3-D velocity model. Plate 7 displays the inversion results for this experiment using various smoothing values. Again, we have performed the inversions with and without timing corrections. As in both of the previous examples, the addition of timing corrections to the GFs significantly improves the resolution of the slip distribution. This allows the inversion to more accurately place a larger portion of slip on the shallower asperity and reduce the spurious slip along the fault edges (Plate 7). The spatial slip correlation goes from 0.65 to 0.85 with the addition of the timing corrections. Figure 9 compares the observed and synthetic ground motions for the time-corrected inversion using a smoothing value of 0.01. The waveform correlation coefficient for this result is 0.72 and the peak amplitude error is 0.253, which compare favorably to the values of 0.60 and 0.399, respectively, that are obtained without timing corrections.

Comparing the results from Plate 6 (SCEC V1 observations) and Plate 7 (Graves observations), we see that although there are differences in the details of the slip distributions, overall, the results are fairly similar. This suggests that the hybrid set of 1-D GFs are not overly sensitive to the uncertainty in the 3-D model, as long as the classification of the stations into basin or rock sites is appropriate.

5. Discussion and Conclusions

The inversion results exhibit varying degrees of success depending on the complexity of the assumed data model and the set of GFs that are used. Table 5 summarizes the goodness of fit measures for the various experiments. Obviously, given a set of ground motion data from a 3-D environment, the best resolution will be obtained using a set of well-calibrated 3-D GFs. Our first inversion exercise considers the end-member case where the 3-D GFs are an exact match to the observations.

The remaining inversion exercises all consider the more typical case where the GFs (either hybrid 1-D or 3-D) are inexact representations of the wave propagation characteristics in the observations. In these situations the introduction of smoothing in the inversion process is necessary due to inaccuracy in the GFs. The better the GFs, the less smoothing that is required. Although we can always improve the fit to the data by reducing the amount of smoothing, in doing this, the slip maximum and slip heterogeneity begin to increase in an unstable fashion. Allowing more complexity in the source, for example by incorporating rake variability, would also greatly improve the fit. However, this is simply mapping inadequacy in the GFs back into the source. Since we never have perfect GFs in the situation with real data, simply using the fit to the observations to gauge the success of the inversion can be problematic.

In the case where we use data from the SCEC V1 3-D model with GFs from the Graves 3-D model, the inversion produces a reduction in the slip resolution compared to the exact case. The decrease in resolution is directly related to the differences in 3-D wave propagation characteristics of the two velocity structures. These two models tend to have their largest differences in the region covered by our study area, and, in a sense, they may represent the end-member cases of relatively complex 3-D structural variability (SCEC V1) versus relatively simple 3-D structural variability (Graves), as evidenced in Plate 2. Thus the results of our inversion exercise illustrate the degree of resolution that can be obtained in the nonoptimal situation of using a set of inexact 3-D GFs.

Our results also reaffirm that the resolution of the 3-D inversion can be increased by improving the accuracy of the 3-D GFs through the refinement of the 3-D velocity structure. In contrast to 1-D and 2D models which can be readily tuned to fit a source to station profile, the refinement of existing 3-D models presents a formidable challenge due to the additional complexity in the parameterization of the 3-D structure. This stresses the need for independent validation of the 3-D structure using exercises such as the modeling of ground motion data from aftershocks [e.g., *Haase et al.*, 1996; *Pitarka and Irikura*, 1996; *Scrivner and Helmberger*, 1999] or other small earthquakes [e.g., *Sato et al.*, 1999; L. Eisner and R. W. Clayton, A reciprocity method for multiple source simulations, submitted to *Bulletin of the Seismological Society of America*, 2001].

For the inversion experiments which use the hybrid set of 1-D GFs, the resolution of the slip distribution is comparable to that obtained with the inexact 3-D GFs (see Table 5). In some respects this result should not be surprising because even though the hybrid set of basin and rock 1-D GFs have "simpler" wave propagation characteristics compared to the 3-D GFs, they still retain the first-order impedance effects of the site response. This is particularly true in our experiments since we only use the first 15 s of the waveforms in the inversions. Thus we are concentrating mainly on the direct up going waves from the source, and omitting most of the secondary arrivals that are generated in the 3-D structures (see Figure 4). Expanding the time window used in the inversion potentially allows the use of information in these later arrivals to help constrain the slip distribution with the 3-D GFs. However, this potential can only be realized if the 3-D GFs are well calibrated. Using inexact 3-D GFs with a longer time window can actually degrade the resolution of the inversion quite rapidly since the degree of misfit between GFs from different 3-D (or 1-D) velocity structures can increase significantly at later times into the waveform [e.g., *Sekiguchi et al.*, 2000]. We confirmed this by performing an inversion with the inexact 3-D GFs using a 25 s time window. The results indicate a significant reduction both in the resolution of slip and in the fit to the observed waveforms compared to the results for the 15 s time window.

The use of hybrid 1-D GFs has been previously

shown to yield significantly better waveform fits than the use of a single set of 1-D GFs which are common to all stations [e.g., *Wald and Heaton*, 1994; *Wald et al.*, 1996]. However, even when using hybrid 1-D models to represent a range of profiles, the resolution potential of the inversion is still inherently limited because the hybrid 1-D GFs can never fully represent the actual 3-D response at a given station. This is true even in the limit that a different 1-D model is used for each site. Clearly, for regions like southern California, the ability to use a set of well-calibrated 3-D GFs to model observed ground motion data is desirable.

The results we present here must be considered within their context. First, the rupture scenario that we analyze in this study represents only a single possible example of faulting in a basin environment. Since the fault plane is located deep beneath the San Fernando basin, the first 10 to 15 s of energy arriving at sites in the near-fault region are dominated by direct up going waves from the source, and the wave propagation effects due to 3-D structure (e.g., basin edge effects, surface wave generation) tend to be minimized [e.g., *Somerville et al.*, 1996; *Hartzell et al.*, 1999]. Other rupture scenarios, such as shallow faulting which occurred in the 1971 San Fernando earthquake, or basin edge faulting which occurred in the 1995 Kobe earthquake have produced very strong 3-D effects at sites in the near fault region. Furthermore, the potential for interaction between source and 3-D wave propagation effects will certainly be greater as the size of the event and duration of rupture increase. These cases need to be examined in greater detail in order to more fully understand the potential benefits and pitfalls of using 3-D GFs in the inversion procedure.

Second, further work is required to consider a more complex rupture process which also allows variability in slip direction, risetime, and rupture velocity across the fault. A number of source inversion studies have demonstrated the importance of incorporating variability in these parameters in order to better resolve the details of the source process [e.g., *Hartzell and Heaton*, 1983; *Cotton and Campillo*, 1995; *Sekiguchi et al.*, 1996]. However, doing this increases the number of free parameters in the inversion procedure, and the effect of this on the resolution potential of the 1-D and 3-D GFs needs to be investigated.

Last, the strong motion waveforms typically used in source inversion analyses sample only a limited bandwidth of data, usually between 1 and 5 s period for M_w 6 to 7 earthquakes. The combined use of strong motion recordings with other data sets such as teleseismic observations or geodetic measurements can greatly increase the period band covered by the inversion. This approach is particularly useful when considering complex, multiparameter rupture models [e.g., *Wald and Heaton*, 1994; *Wald et al.*, 1996; *Yoshida et al.*, 1996]. In many cases these different data sets are complementary. For example, geodetic measurements can provide valuable constraints on the final slip distribution, but are insensitive to the time evolution of slip. On the other hand, strong motion waveforms can provide detailed information on the temporal evolution of the rupture process, but are not as sensitive to the final static deformation. Combining these data sets in the inversion procedure provides a greater degree of stability and results in a more comprehensive and robust model of the rupture process [e.g., *Wald and Heaton*, 1994; *Wald and Somerville*, 1995; *Wald and Graves*, 1999]. A detailed investigation of combined data set source inversions using 1-D and 3-D GFs is presented as a companion paper to this work [*Wald and Graves*, this issue].

Acknowledgments. Discussions with Hiroshi Kawase and Toshiaki Sato throughout the course of this work were very beneficial. The authors are also grateful for the constructive review comments provided by Rachel Abercrombie, Steve Day, Steve Hartzell, and Susan Hough. Several of the figures for the manuscript were prepared using GMT software [*Wessel and Smith*, 1991]. This work was sponsored in part by USGS external program grants 1434-HQ-97-GR-03023 and 99-HQ-GR-0088.

References

Aki, K., and P. G. Richards, *Quantitative Seismology*, 932 pp., W. H. Freeman, New York, 1980.

Beroza, G. C., Near-source modeling of the Loma Prieta earthquake: Evidence for heterogeneous slip and implications for earthquake hazard, *Bull. Seismol. Soc. Am., 81*, 1603-1621, 1991.

Brocher, T. M., et al., A crustal-scale 3D seismic velocity model for the San Francisco Bay area, California (abstract), *Eos Trans. AGU, 78*(46), Fall Meet. Suppl., F435-F436, 1997.

Cohee, B. P., and G. C. Beroza, Slip distribution of the 1992 Landers earthquake and its implications for earthquake source mechanics, *Bull. Seismol. Soc. Am., 84*, 692-712, 1994.

Cotton, F., and M. Campillo, Frequency domain inversion of strong motions: Application to the 1992 Landers earthquake, *J. Geophys. Res., 100*, 3961-3975, 1995.

Dahlen, F. A., and J. Tromp, *Theoretical Global Seismol-*

ogy, 1025 pp., Princeton Univ. Press, Princeton, N.J., 1998.

Frankel, A., Three-dimensional simulations of ground motions in the San Bernardino Valley, California, for hypothetical earthquakes on the San Andreas fault, *Bull. Seismol. Soc. Am., 83*, 1020-1041, 1993.

Frankel, A., and J. E. Vidale, A three dimensional simulation of seismic waves in the Santa Clara Valley, California, from a Loma Prieta aftershock, *Bull. Seismol. Soc. Am., 82*, 2045-2074, 1992.

Gao, S., H. Liu, P. M. Davis, and L. Knopoff, Localized amplification of seismic waves and correlation with damage due to the Northridge earthquake: Evidence for focusing in Santa Monica, *Bull. Seismol. Soc. Am., 86*, S209-S230, 1996.

Graves, R. W., Simulating realistic earthquake ground motions in regions of deep sedimentary basins, paper presented at 11th World Conference on Earthquake Engineering, Int. Assoc. for Earthquake Eng., Acapulco, Mexico, 1996a.

Graves, R. W., Simulating seismic wave propagation in 3D elastic media using staggered grid finite differences, *Bull. Seismol. Soc. Am., 86*, 1091-1106, 1996b.

Graves, R. W., Three dimensional finite difference modeling of the San Andreas fault: Source parameterization and ground motion levels, *Bull. Seismol. Soc. Am., 88*, 881-897, 1998.

Graves, R. W., and R. W. Clayton, Modeling path effects in three-dimensional basin structures, *Bull. Seismol. Soc. Am., 82*, 81-103, 1992.

Guatteri, M., and P. Spudich, What can strong motion data tell us about slip weakening fault friction laws?, *Bull. Seismol. Soc. Am., 90*, 98-116, 2000.

Haase, J. S., E. Hauksson, F. Vernon, and A. Edelman, Modeling of ground motion from a 1994 Northridge aftershock using a tomographic velocity model of the Los Angeles basin, *Bull. Seismol. Soc. Am., 86*, S156-S167, 1996.

Hartzell, S. H., and T. H. Heaton, Inversion of strong ground motion and teleseismic waveform data for the fault rupture history of the 1979 Imperial Valley, California earthquake, *Bull. Seismol. Soc. Am., 73*, 1553-1583, 1983.

Hartzell, S., P. Liu, and C. Mendoza, The 1994 Northridge, California earthquake: Investigation of rupture velocity, risetime, and high-frequency radiation, *J. Geophys. Res., 101*, 20,091-20,108, 1996.

Hartzell, S., E. Cranswick, A. Frankel, D. Carver, and M. Meremonte, Variability of site response in the Los Angeles urban area, *Bull. Seismol. Soc. Am., 87*, 1377-1400, 1997.

Hartzell, S., S. Harmsen, A. Frankel, and S. Larsen, Calculation of broadband time histories of ground motion: Comparison of methods and validation using strong ground motion from the 1994 Northridge earthquake, *Bull. Seismol. Soc. Am., 89*, 1484-1504, 1999.

Iida, M., Source effects on strong motion records and resolving power of strong motion arrays for source inversion, *Tectonophysics*, *218*, 179-193, 1993.

Liu, P., and R. J. Archuleta, Source parameter inversion using 3D Green's functions: Application to the 1996 Northridge, California earthquake (abstract), *Eos Trans. AGU, 80*(46), Fall Meet. Suppl., F709, 1999.

Magistrale, H., R. Graves, and R. Clayton, A standard three-dimensional seismic velocity model for southern California: Version 1 (abstract), *Eos Trans. AGU, 79*(46), Fall Meet. Suppl., F605, 1998.

Olsen, K. B., and R. J. Archuleta, Three-dimensional simulation of earthquakes on the Los Angeles fault system, *Bull. Seismol. Soc. Am., 86*, 575-596, 1996.

Pitarka, A., and K. Irikura, Basin structure effects on long period strong motions in the San Fernando valley and the Los Angeles basin from the 1994 Northridge earthquake and an aftershock, *Bull. Seismol. Soc. Am., 86*, S126-S137, 1996.

Pitarka, A., K. Irikura, T. Iwata, and H. Sekiguchi, Three dimensional simulation of the near fault ground motion for the 1995 Hyogo-ken Nanbu (Kobe), Japan earthquake, *Bull. Seismol. Soc. Am., 88*, 428-440, 1998.

Saikia, C. K., Modified frequency-wavenumber algorithm for regional seismograms using Filon's quadrature: Modelling of L_g waves in eastern North America, *Geophys. J. Int.*, *118*, 142-158, 1994.

Sarao, A., S. Das, and P. Suhadolc, Effect of non-uniform station coverage on the inversion for earthquake rupture history for a Haskell-type source model, *J. Seismol.*, *2*, 1-25, 1998.

Sato, T., R. W. Graves, and P. G. Somerville, Three dimensional finite difference simulations in the Tokyo metropolitan area during the 1990 Odawara earthquake (M_J 5.1) and the great 1923 Kanto earthquake (M_S 8.2) in Japan, *Bull. Seismol. Soc. Am., 89*, 579-607, 1999.

Scrivner, C. V., and D. V. Helmberger, Finite difference modeling of two aftershocks of the 1994 Northridge, California earthquake, *Bull. Seismol. Soc. Am., 89*, 1505-1518, 1999.

Sekiguchi, H., K. Irikura, T. Iwata, Y. Kakehi, and M. Hoshiba, Minute locating of fault planes and source process of the 1995 Hyogoken-nanbu earthquake from the waveform inversion of strong ground motion, *J. Phys. Earth*, *44*, 473-487, 1996.

Sekiguchi, H., K. Irikura, and T. Iwata, Fault geometry at the rupture termination of the 1995 Hyogo-ken Nanbu earthquake, *Bull. Seismol. Soc. Am., 90*, 117-134, 2000.

Somerville, P. G., R. W. Graves, and C. K. Saikia, Characterization of ground motions during the Northridge earthquake of January 17, 1994, *SAC Rep. 95-03*, 179 pp., Appl. Technol. Counc., Redwood City, Calif., 1995.

Wald, D. J., Slip history of the 1995 Kobe, Japan, earthquake determined from strong motion, teleseismic, and

geodetic data, *J. Phys. Earth*, *44*, 489-503, 1996.

Wald, D. J., and R. W. Graves, The seismic response of the Los Angeles basin, California, *Bull. Seismol. Soc. Am., 88*, 337-356, 1998.

Wald, D. J., and R. W. Graves, On the importance of 3D Earth structure for recovering the earthquake source rupture process (abstract), *Eos Trans. AGU, 80*(46), Fall Meet. Suppl., F933, 1999.

Wald, D. J., and R. W. Graves, Resolution analysis of finite fault source inversion using one- and three-dimensional Green's functions, 2, Combining seismic and geodetic data, *J. Geophys. Res.,* this issue.

Wald, D. J., and T. H. Heaton, Spatial and temporal distribution of slip for the 1992 Landers, California, earthquake, *Bull. Seismol. Soc. Am., 84*, 668-691, 1994.

Wald, D. J., and P. G. Somerville, Variable-slip rupture model of the great 1923 Kanto, Japan earthquake: Geodetic and body-waveform analysis, *Bull. Seismol. Soc. Am., 85*, 159-177, 1995.

Wald, D. J., T. H. Heaton and D. V. Helmberger. Rupture model of the 1989 Loma Prieta earthquake from the inversion of strong motion and broadband teleseismic data, *Bull. Seismol. Soc. Am., 81*, 1540-1572, 1991.

Wald, D. J., T. H. Heaton, and K. W. Hudnut, The slip history of the 1994 Northridge, California, earthquake determined from strong motion, teleseismic, GPS, and leveling data, *Bull. Seismol. Soc. Am., 86*, S49-S70, 1996.

Wessel, P., and W.H.F. Smith, Free software helps map and display data, *Eos Trans. AGU, 72*, 441, 445-446, 1991.

Yoshida, S., K. Koketsu, B. Shibazaki, T. Sagiya, T. Kato, and Y. Yoshisa, Joint inversion of near- and far-field waveforms and geodetic data for the process of the 1995 Kobe earthquake, *J. Phys. Earth*, *44*, 437-454, 1996.

Zeng, Y., and J. G. Anderson, A composite source model of the 1994 Northridge earthquake using genetic algorithms, *Bull. Seismol. Soc. Am., 86*, S71-S83, 1996.

R. Graves, URS Corporation, 566 El Dorado Street, Pasadena, CA 91101. (robert_graves@urscorp.com)

D. Wald, U.S. Geological Survey, 525 South Wilson Avenue, Pasadena, CA 91106. (wald@usgs.gov)

Received March 28, 2000; revised November 21, 2000; accepted November 30, 2000.

This preprint was prepared with AGU's LaTeX macros v5.01. File inv3d˙r2 formatted May 14, 2004.

Figure 1. (left) Map view of the finite difference (FD) model used in the reciprocal Green's function (RGF) test calculations. The basis for this model is the San Fernando basin region of southern California. The three hypothetical source locations (e01, e02, and e03) are denoted with stars and the observation site (s01) is shown with a triangle. (right) Vertical cross sections showing shear wave velocity along profiles A-A' and B-B' through the FD model. The velocity structure is from the model of *Graves* [1996a].

Figure 2. Comparison of velocity time histories computed with the staggered grid FD method using the RGF approach (solid line) and direct solution (dashed line) for the three hypothetical point sources. The results are in very good agreement with one another.

Figure 3. Map showing the San Fernando basin region used in the finite fault inversion experiments. The surface projection of the assumed fault plane is shown by the dashed rectangle (heavy line along top edge). The locations of the two slip blocks (hatched shading) and the epicenter (star) are also indicated. Locations of strong motion stations are shown by triangles. The extent of the FD model grid is given by the large box, along with the locations of cross sections A-A', B-B', and C-C'.

Figure 4a. Horizontal component ground velocity time histories simulated at each of the strong motion sites with the prescribed rupture model using the two 3-D velocity structures as well as the site-specific 1-D (rock or basin) velocity structure. For each station, two sets of three time histories are shown. The top set of seismograms are for the north component and the bottom set are for the east component. Within each component set, the top trace is from the Graves 3-D model, the middle trace is from the SCEC V1 3-D model, and the bottom trace is from the 1-D model. Rock sites are shown in Figure 4a, basin sites are shown in Figures 4b and 4c. A low-pass filter with a corner at 0.667 Hz has been applied to these records. The peak velocity (cm/s) is shown to the right of each trace.

Figure 4b. Same as Figure 4a.

Figure 4c. Same as Figure 4a.

Figure 5. Comparison of observed (SCEC V1 3-D) and predicted ground motions (SCEC V1 3-D) from the inversion using smoothing value of 0.01. Observations are solid lines, and synthetics are dashed lines. The waveform correlation coefficient and peak amplitude misfit error are given in the top right of the figure.

Plate 1. Slip distribution used in the forward simulations. Slip amount is contoured in meters and the hypocenter is indicated by the star. The shallow asperity has a constant 2 m of slip, and the deep asperity has a constant 1 m of slip. All other regions of the fault have zero slip.

Plate 2. Vertical cross sections showing shear wave velocity along profiles A-A', B-B', and C-C' for both the Graves and Southern California Earthquake Center version 1 (SCEC V1) 3-D velocity models. The white line in profiles A-A' and B-B' shows the intersection of the shallow asperity from the prescribed slip model with the cross sections.

Plate 3. One-dimensional velocity models for (left) rock sites and (right) basin sites for (top) the SCEC V1 model and (bottom) the Graves model. The heavy black line shows the generic 1-D model used for the inversion analysis.

Plate 4. Inversion results for SCEC V1 3-D observations and SCEC V1 3-D GFs. (a) The input slip model. (b) Inversion results with no smoothing constraints. Since the RGFs are from the same 3-D velocity model that is used to generate the observations, the inversion fully recovers the exact slip distribution. (c and d) Inversion results with smoothing values of 0.005 and 0.01, respectively.

Figure 6. Comparison of the effect of time shifting of the GFs prior to the inversion at stations jens, nwhp, and pard. Results obtained (left) without time corrections and (right) with time corrections. Observations are solid lines, and synthetics are dashed lines. All results are for a smoothing value of 0.01.

Figure 7. Comparison of observed (SCEC V1 3-D) and predicted ground motions (Graves 3-D) from the inversion using smoothing value of 0.01. Observations are solid lines, and synthetics are dashed lines. The waveform correlation coefficient and peak amplitude misfit error are given in the top right of the figure.

Figure 8. Comparison of observed (SCEC V1 3-D) and predicted ground motions (hybrid 1-D) from the inversion using smoothing value of 0.01. Observations are solid lines, and synthetics are dashed lines. The waveform correlation coefficient and peak amplitude misfit error are given in the top right of the figure.

Figure 9. Comparison of observed (Graves 3-D) and predicted ground motions (hybrid 1-D) from the inversion using smoothing value of 0.01. Observations are solid lines, and synthetics are dashed lines. The waveform correlation coefficient and peak amplitude misfit error are given in the top right of the figure.

Plate 5. Inversion results for smoothing of (top) 0.0, (middle) 0.005, and (bottom) 0.01 for SCEC V1 3-D observations and Graves 3-D GFs for cases of (left) no time shifting of the GFs prior to the inversion, and (right) time shifting to align first arrivals prior to the inversion.

Plate 6. Inversion results for smoothing of (top) 0.0, (middle) 0.005, and (bottom) 0.01 for SCEC V1 3-D observations and hybrid 1-D GFs for cases of (left) no time shifting of the GFs prior to the inversion, and (right) time shifting to align first arrivals prior to the inversion.

Plate 7. Inversion results for smoothing of (top) 0.0, (middle) 0.005, and (bottom) 0.01 for Graves 3-D observations and rock/basin 1-D GFs for cases of (left) no time shifting of the GFs prior to the inversion, and (right) time shifting to align first arrivals prior to the inversion.

Table 1. Source Parameters for 3-D Reciprocal Green's Function Tests

Source	Strike	Dip	Rake	Depth, km	M_o, N m
e01	47°	70°	20°	1.0	1×10^{17}
e02	126°	30°	105°	5.0	2×10^{17}
e03	267°	45°	60°	7.0	3×10^{17}

Table 2. Fault Model Parameters

Parameter	Value
Top center (TC) location	34.344° N, −118.515° E
Length	18 km
Width	24 km
Depth to top edge	5 km
Strike	122°
Dip	40°
Rake	105°
Rupture velocity	3 km/s
Hypocenter (from TC)	
Along strike	5 km
Downdip	20 km
Risetime	0.6 s
M_w	6.45

Table 3. Strong Motion Stations

Station	Name	Latitude, °N	Longitude, °E	Site Type
Canoga Park	cnpk	34.212	-118.601	basin
Energy Control Center	ecc	34.259	-118.336	rock
Encino Reservoir	encr	34.150	-118.510	rock
Jenson Filtration Plant	jens	34.312	-118.496	basin
Kagel Canyon	kagc	34.288	-118.375	rock
Newhall Fire Department	newh	34.387	-118.530	basin
Newhall Pico Canyon	nwhp	34.391	-118.622	basin
Pacoima Dam	pacd	34.334	-118.396	rock
Pardee Substation	pard	34.435	-118.582	basin
Rinaldi Receiving Station	rrs	34.281	-118.479	basin
Receiving Station East	rse	34.176	-118.360	basin
Canoga Park Saticoy	sati	34.209	-118.517	basin
Sherman Oaks	shrm	34.154	-118.465	basin
Sepulveda VA Hospital	spva	34.249	-118.475	basin
Santa Susanna	ssus	34.231	-118.713	rock
Santa Susanna Katherine	svsc	34.264	-118.666	rock
Sylmar	sylm	34.326	-118.444	basin
Van Nuys	vnuy	34.221	-118.471	basin

Table 4. Finite Difference Modeling Parameters

Parameter	Value
Model grid dimensions	$310 \times 250 \times 180$
Total time steps	4000
Grid spacing, km	0.15
Time step, s	0.008
Minimum velocity, km/s	0.5
Maximum frequency limit, Hz	0.667

Table 5. Goodness of Fit Measures (Smoothing = 0.01)

Data Model	GF Model	Timing Shift	W_{XC}[a]	$\ln(\sigma P_v)$[b]	S_{XC}[c]
SCEC V1 3-D	SCEC V1 3-D	no	0.99	0.059	0.92
SCEC V1 3-D	Graves 3-D	yes	0.78	0.337	0.79
SCEC V1 3-D	Graves 3-D	no	0.64	0.372	0.57
SCEC V1 3-D	Hybrid 1-D	yes	0.76	0.314	0.75
SCEC V1 3-D	Hybrid 1-D	no	0.63	0.485	0.68
Graves 3-D	Hybrid 1-D	yes	0.72	0.253	0.85
Graves 3-D	Hybrid 1-D	no	0.60	0.399	0.65

[a] W_{XC} denotes waveform cross-correlation coefficient.

[b] σP_v denotes standard error in misfit to peak velocity.

[c] S_{XC} denotes slip distribution correlation coefficient.

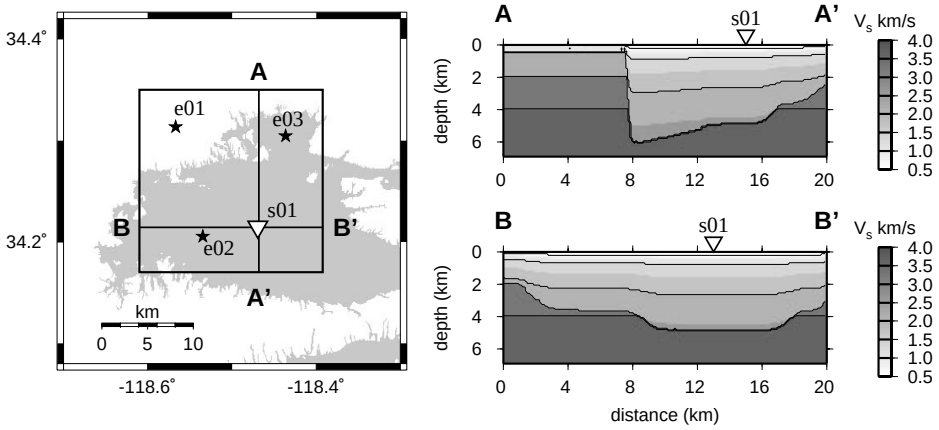

Figure 1: DOUBLE column width, BLACK AND WHITE.

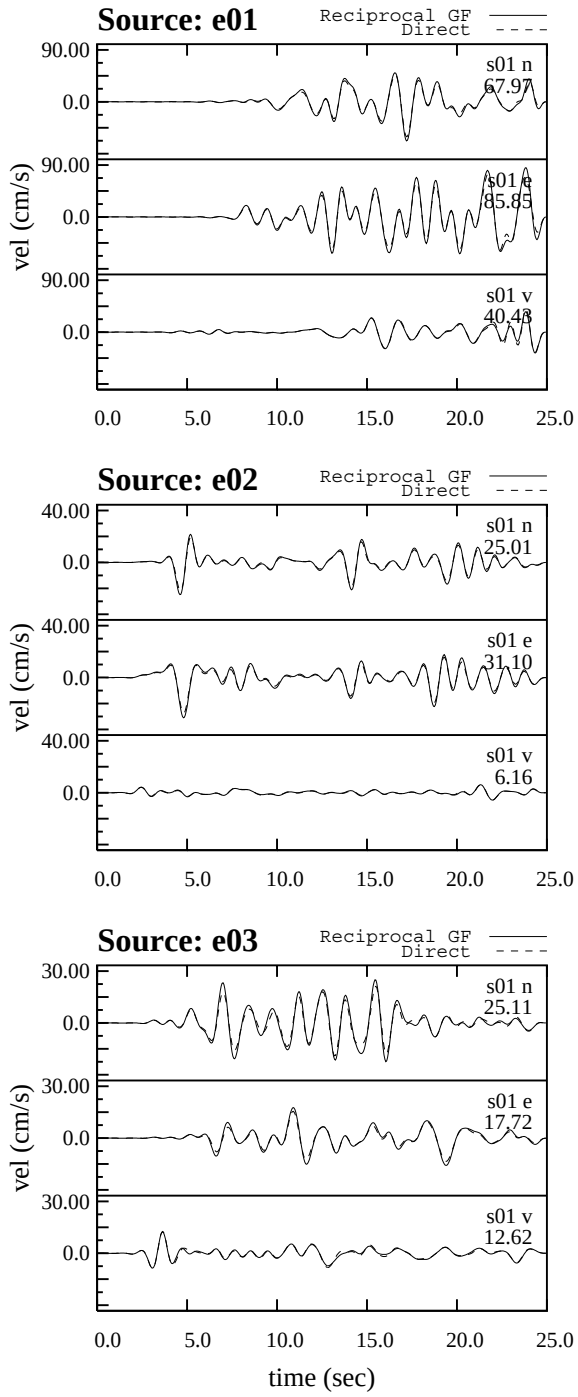

Figure 2: SINGLE column width, BLACK AND WHITE.

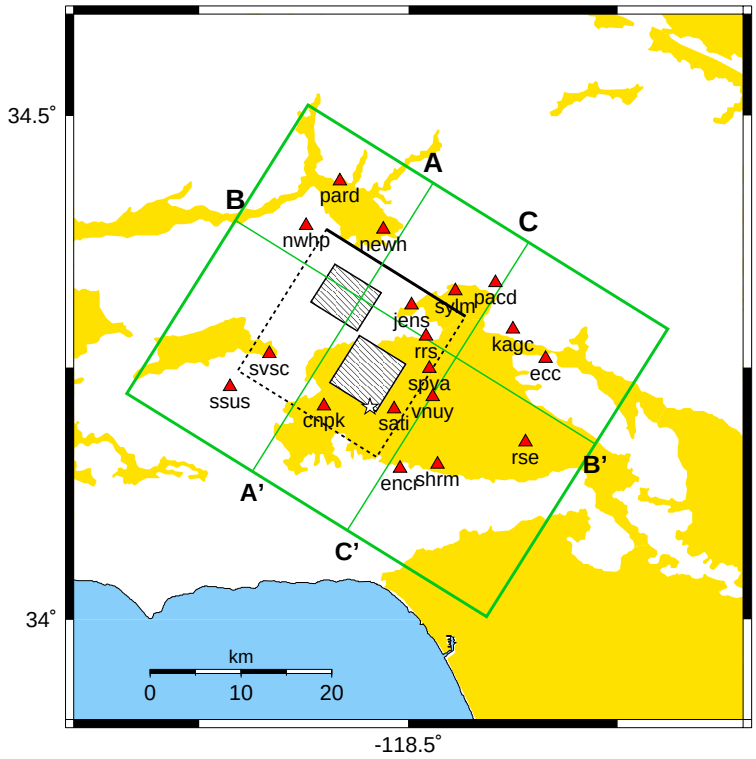

Figure 3: DOUBLE column width, BLACK AND WHITE.

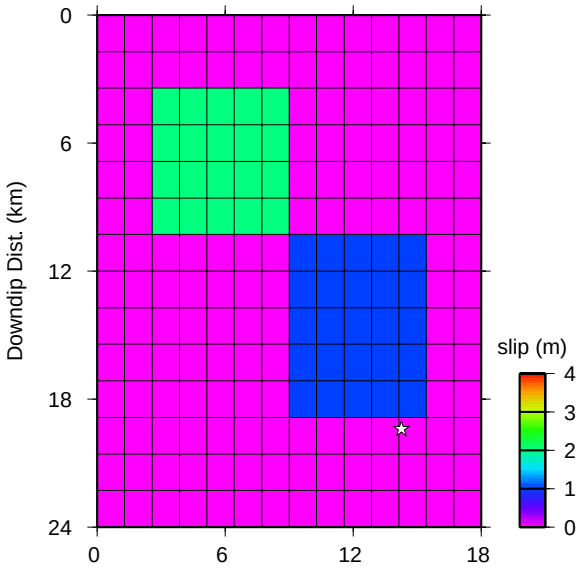

Plate 1: SINGLE column width, COLOR.

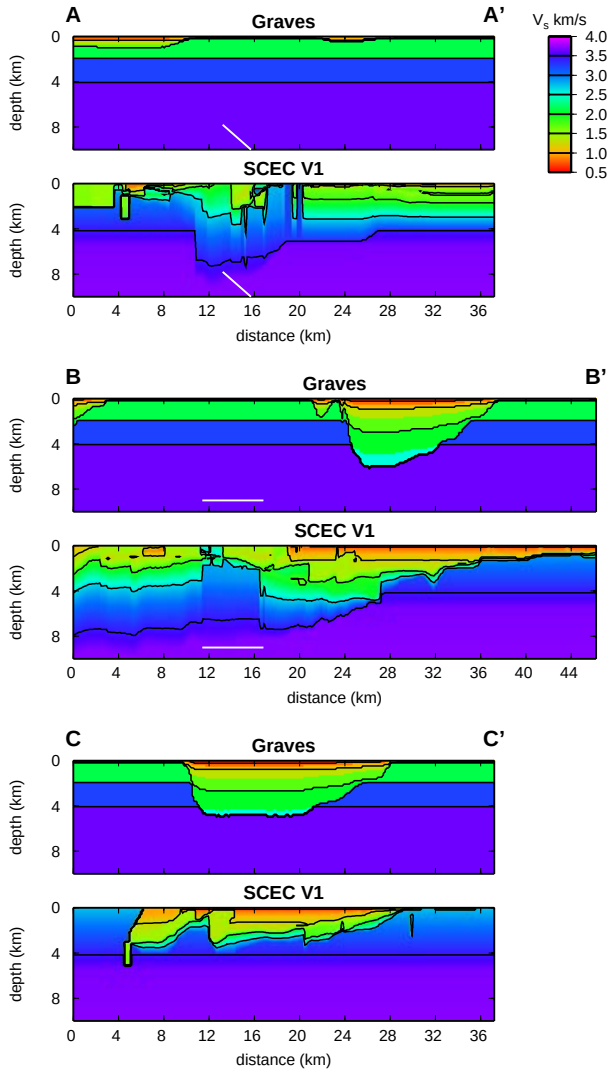

Plate 2: SINGLE column width, COLOR.

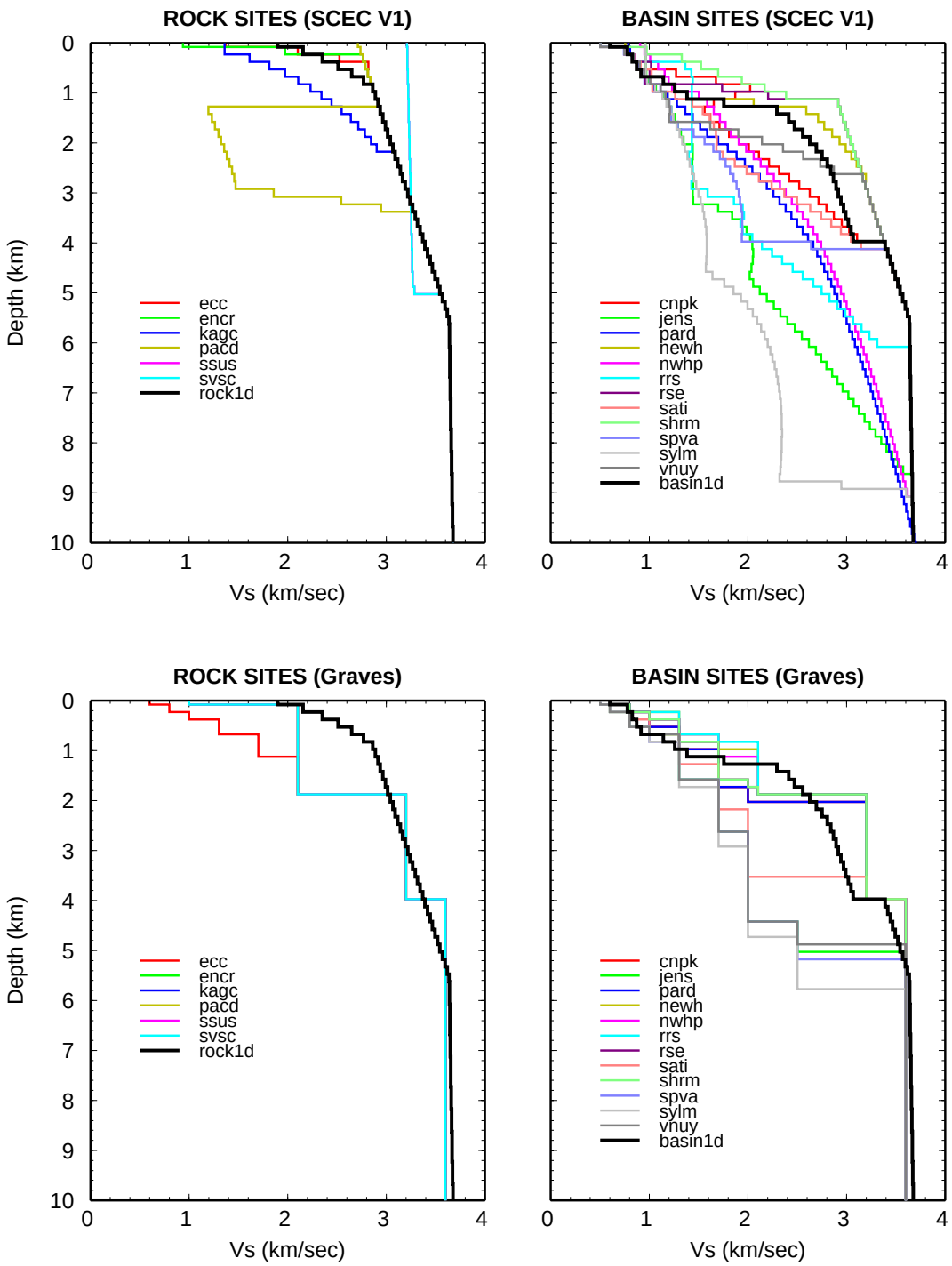

Plate 3: DOUBLE column width, COLOR.

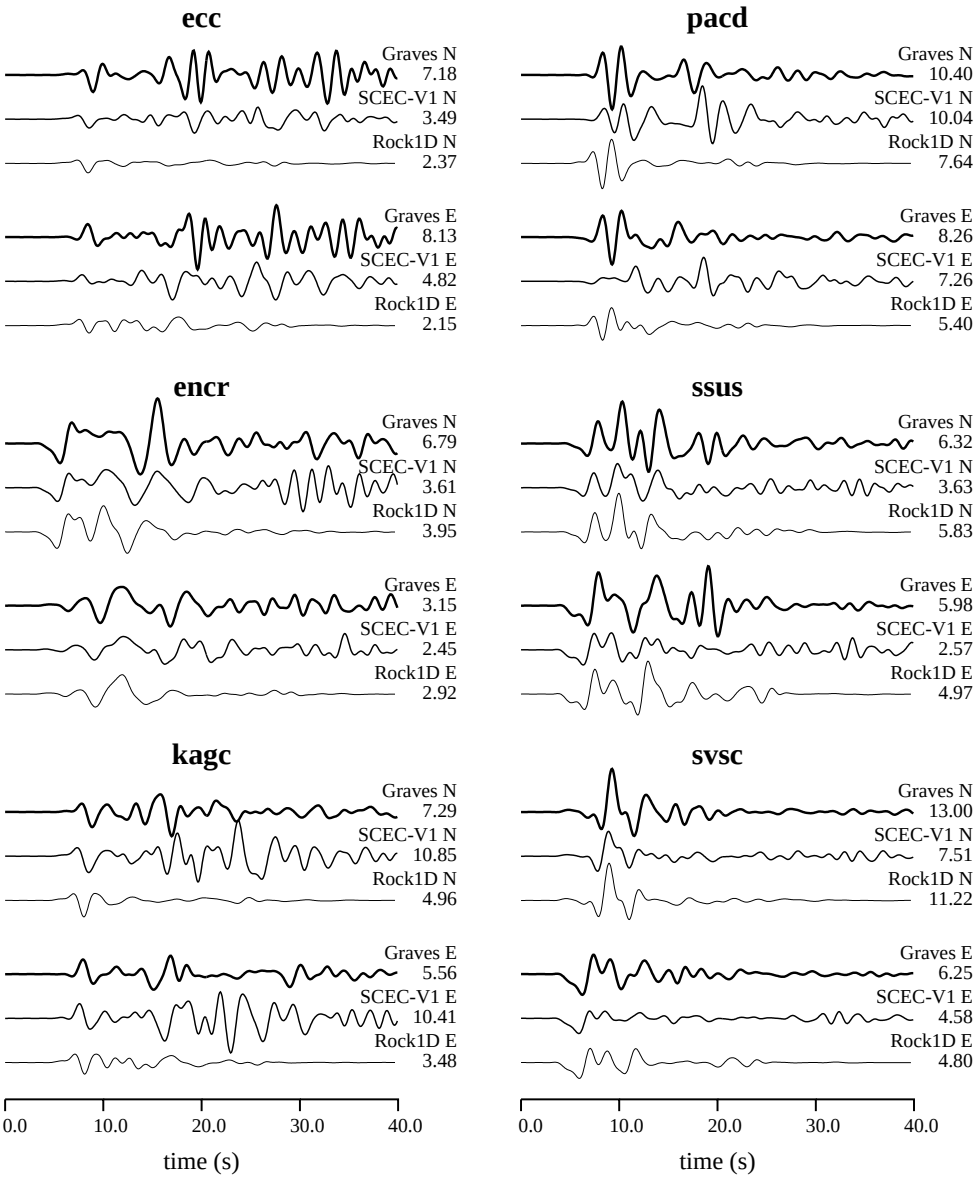

Figure 4a: DOUBLE column width, BLACK AND WHITE.

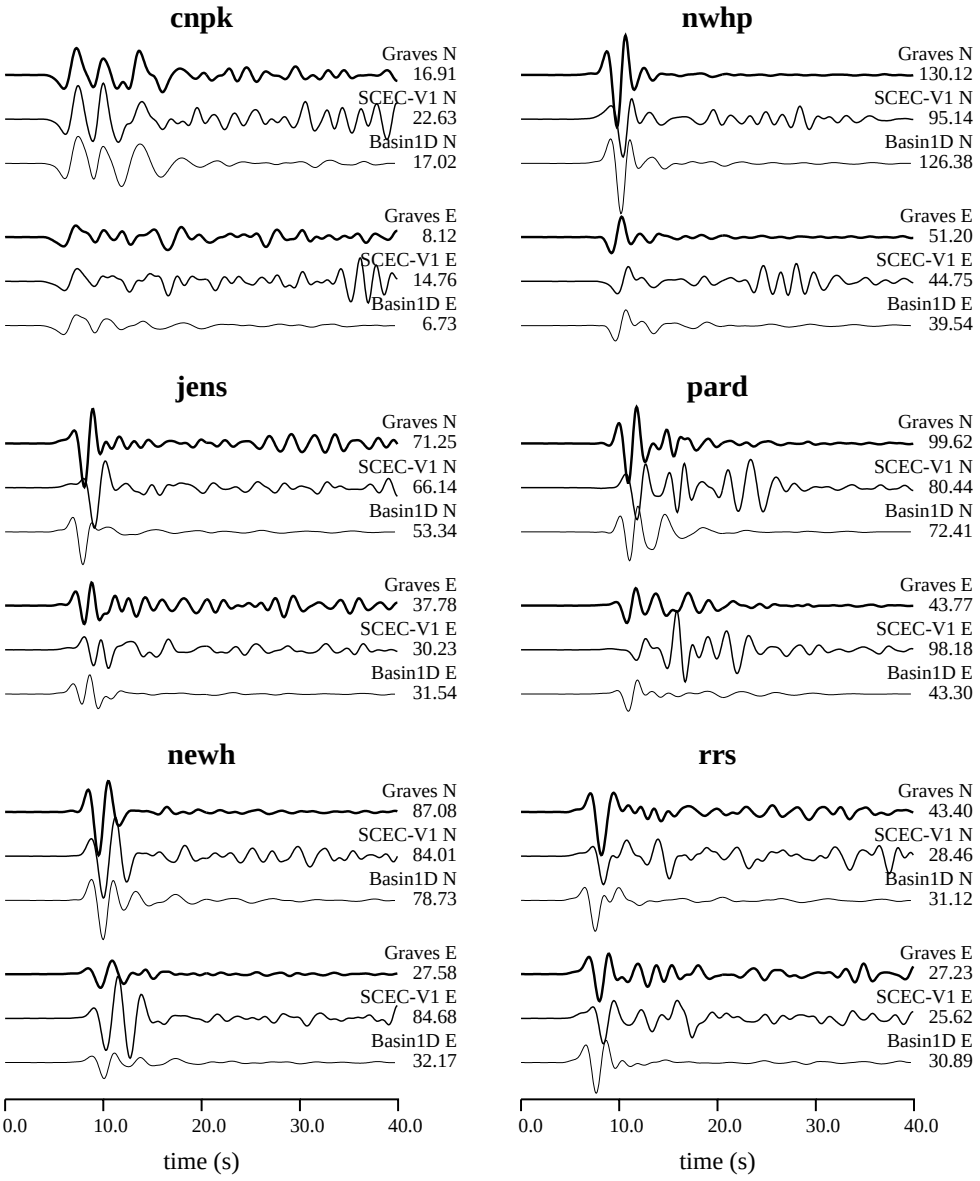

Figure 4b: DOUBLE column width, BLACK AND WHITE.

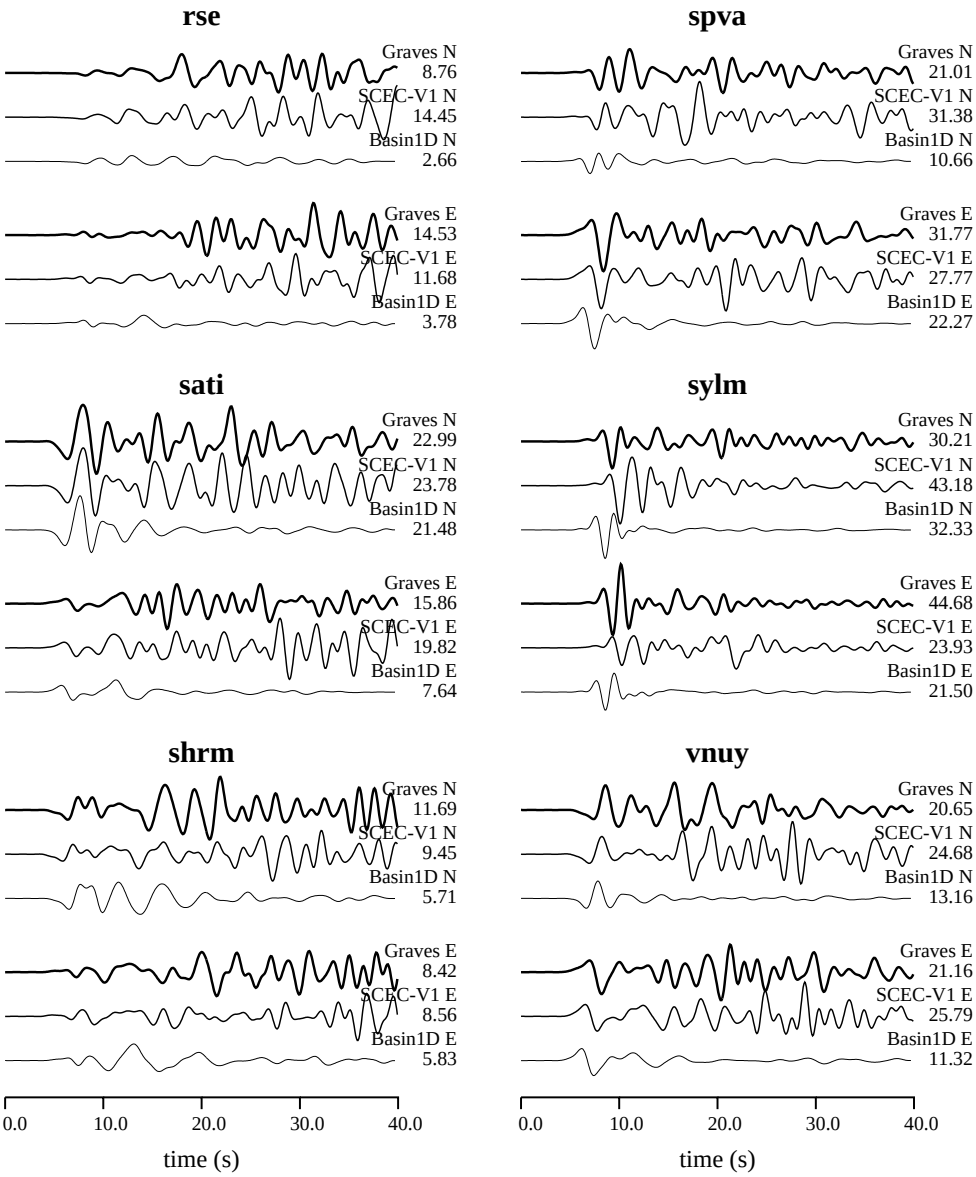

Figure 4c: DOUBLE column width, BLACK AND WHITE.

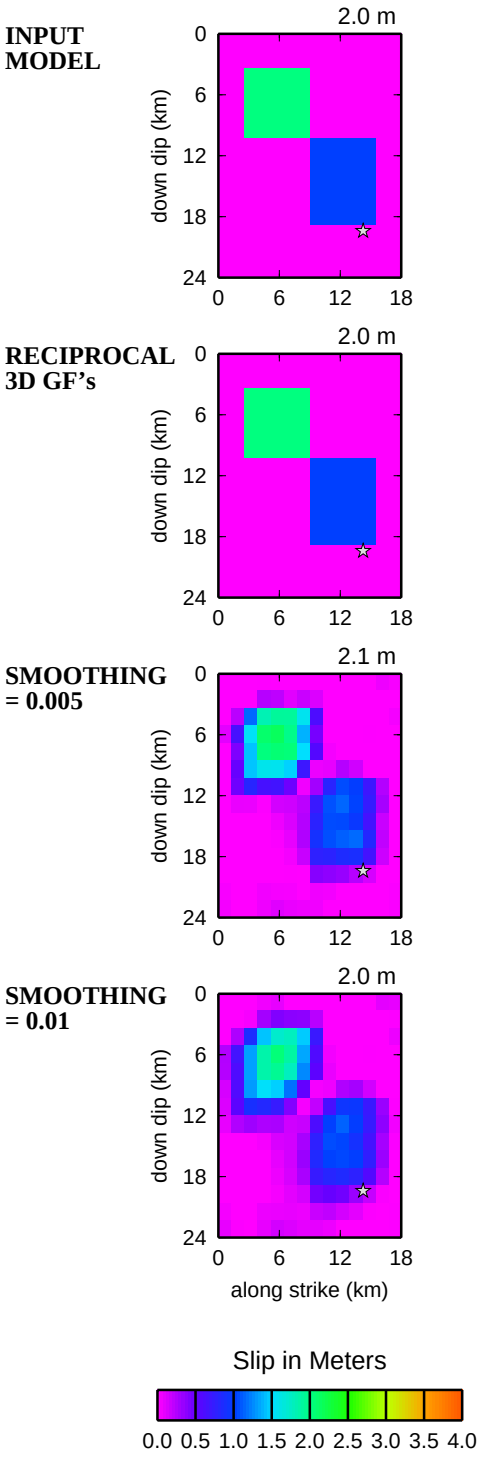

Plate 4: SINGLE column width, COLOR.

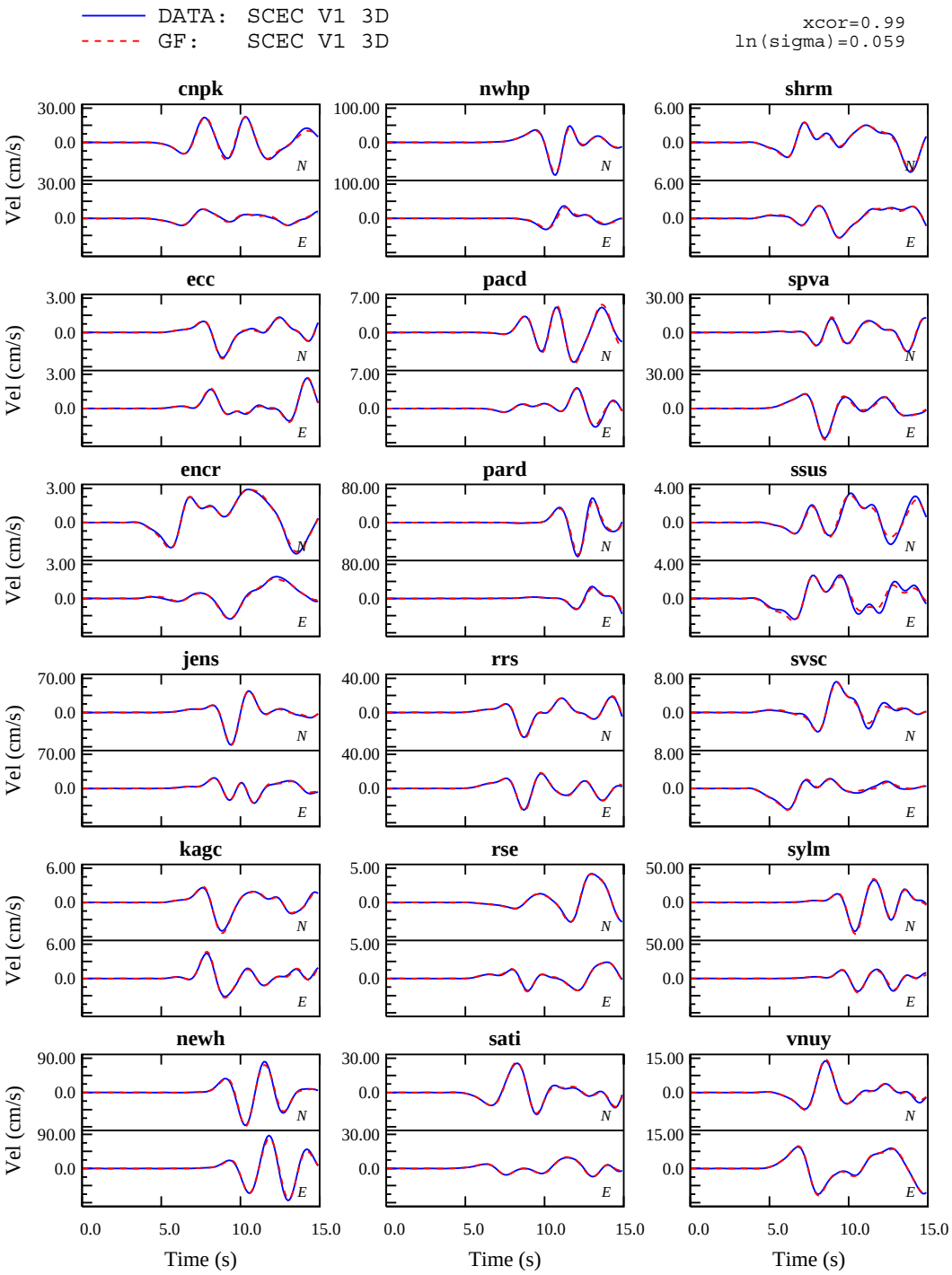

Figure 5: DOUBLE column width, BLACK AND WHITE.

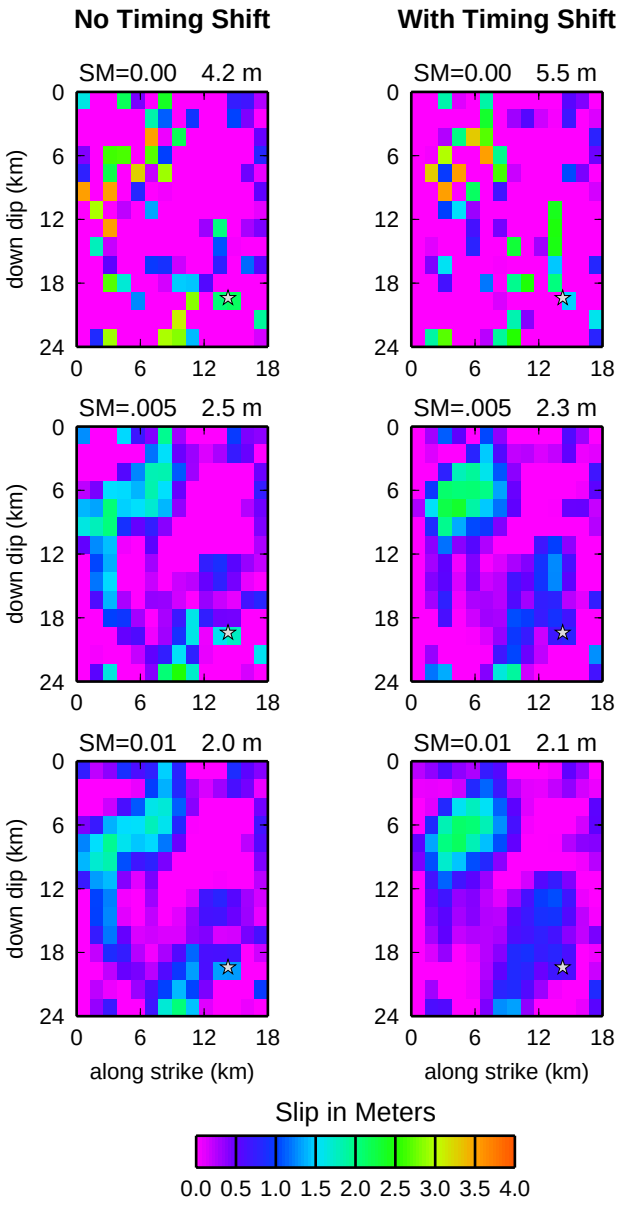

Plate 5: SINGLE column width, COLOR.

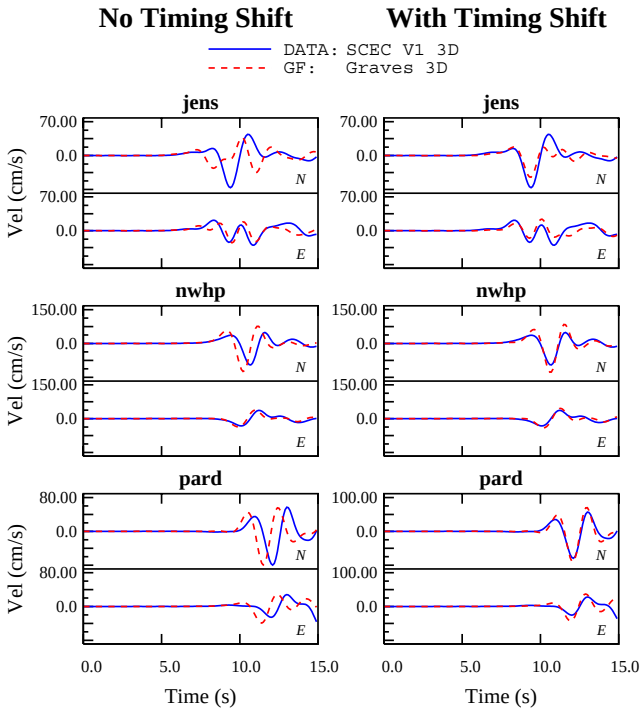

Figure 6: SINGLE column width, BLACK AND WHITE.

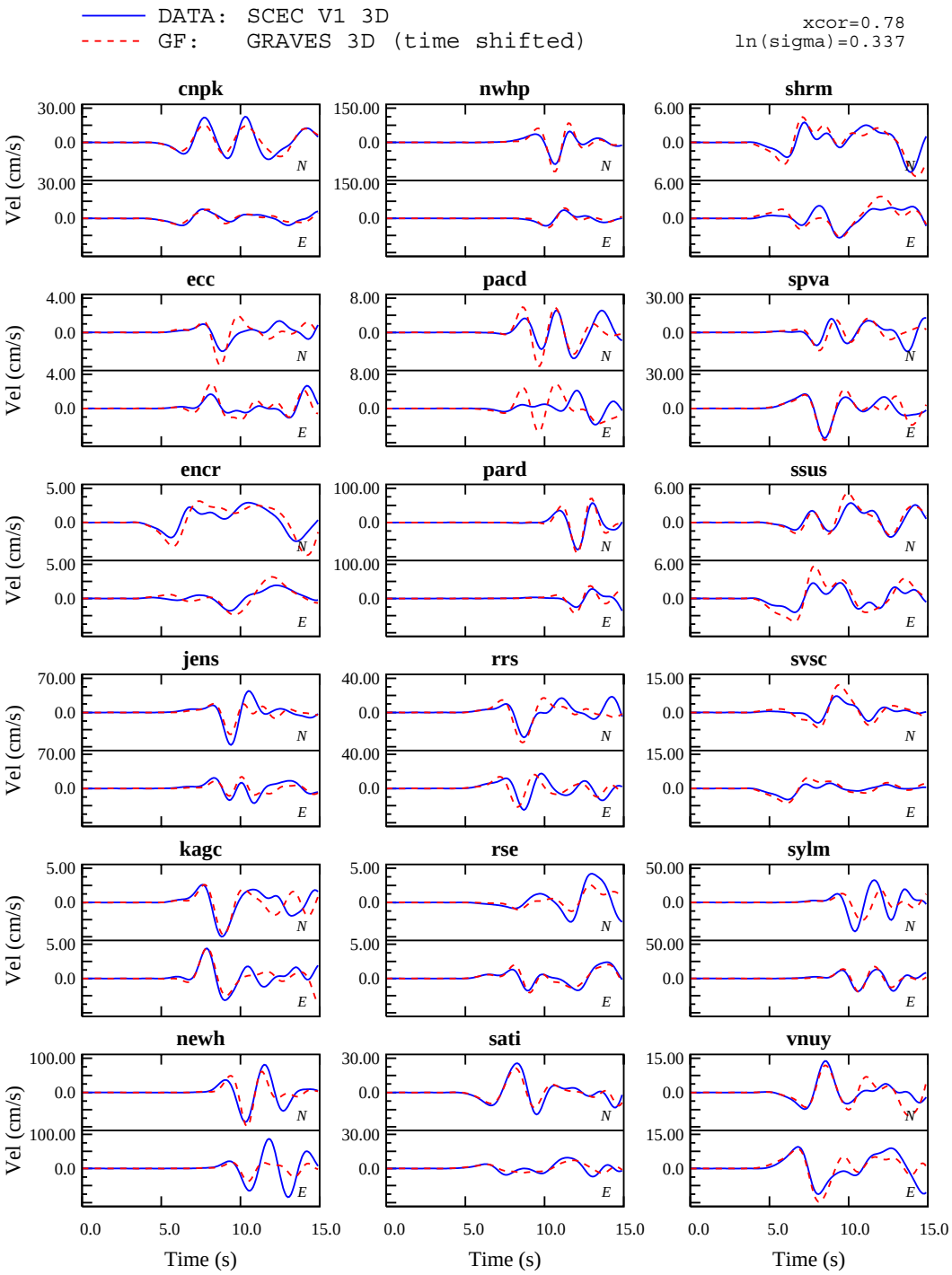

Figure 7: DOUBLE column width, BLACK AND WHITE.

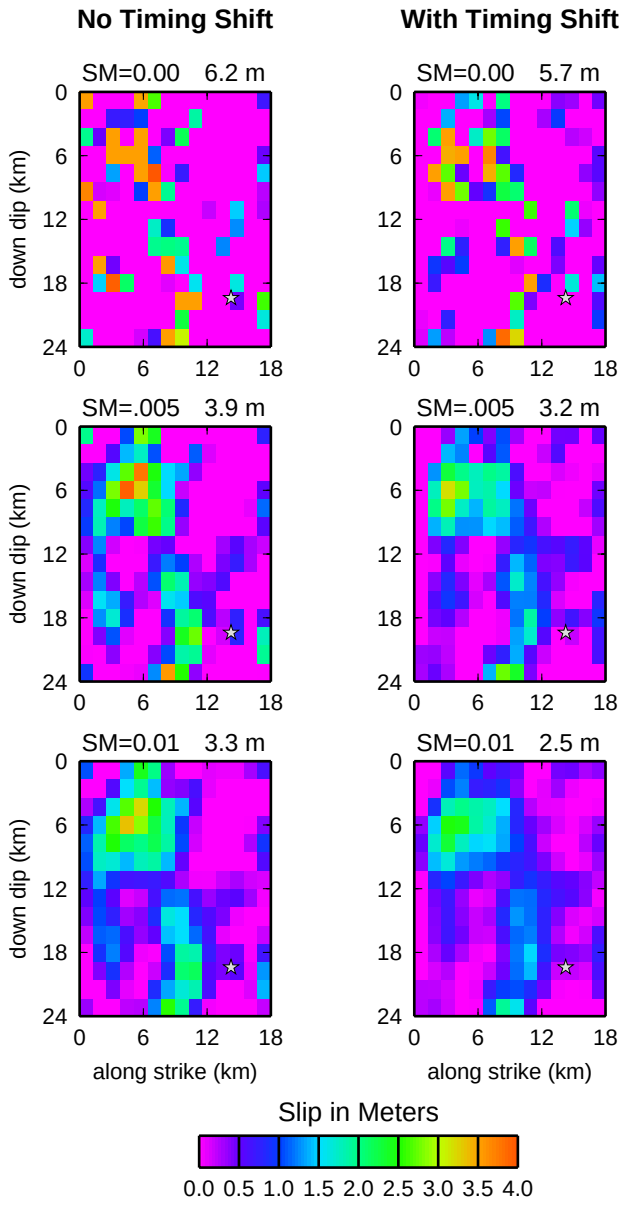

Plate 6: SINGLE column width, COLOR.

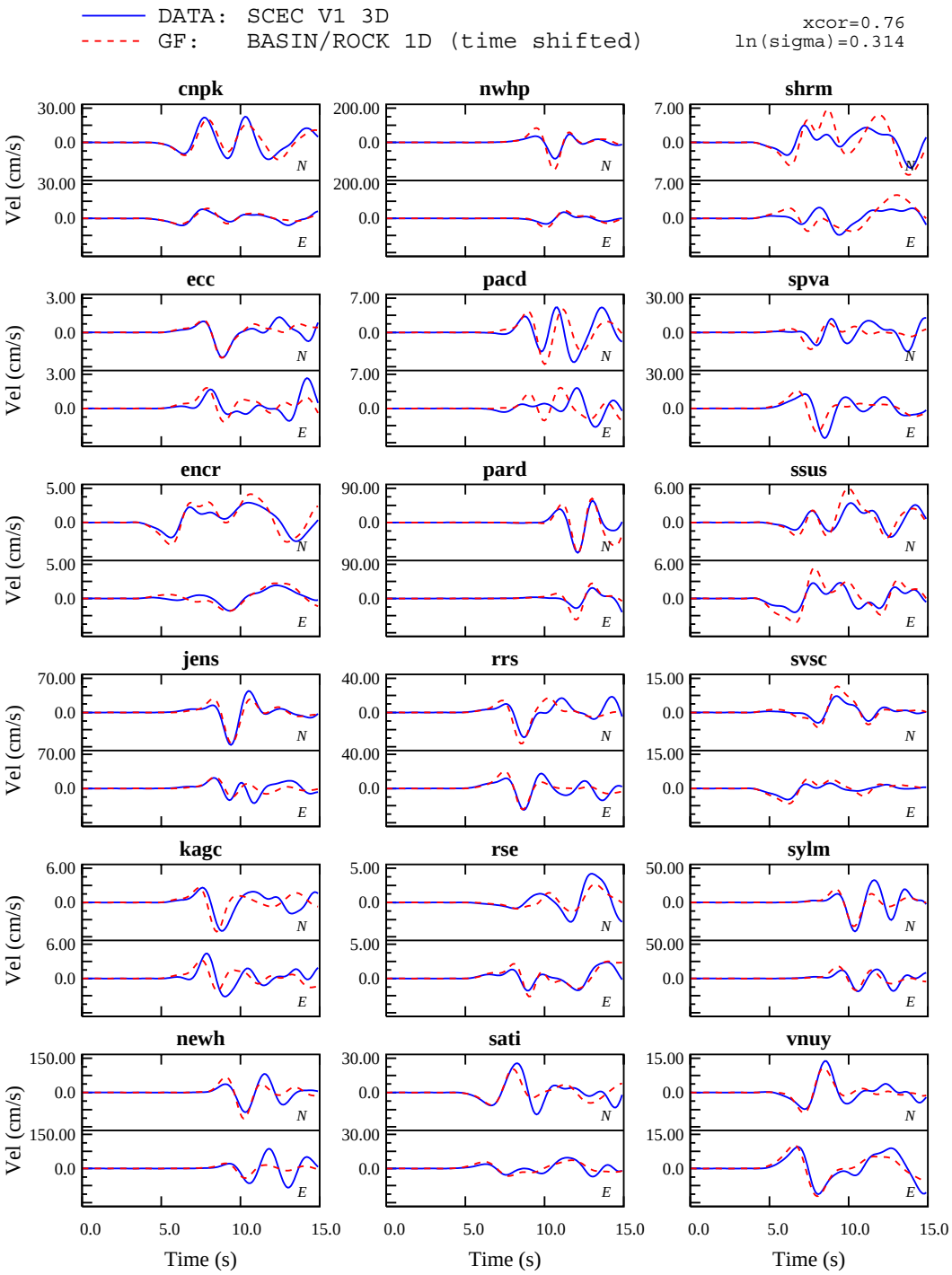

Figure 8: DOUBLE column width, BLACK AND WHITE.

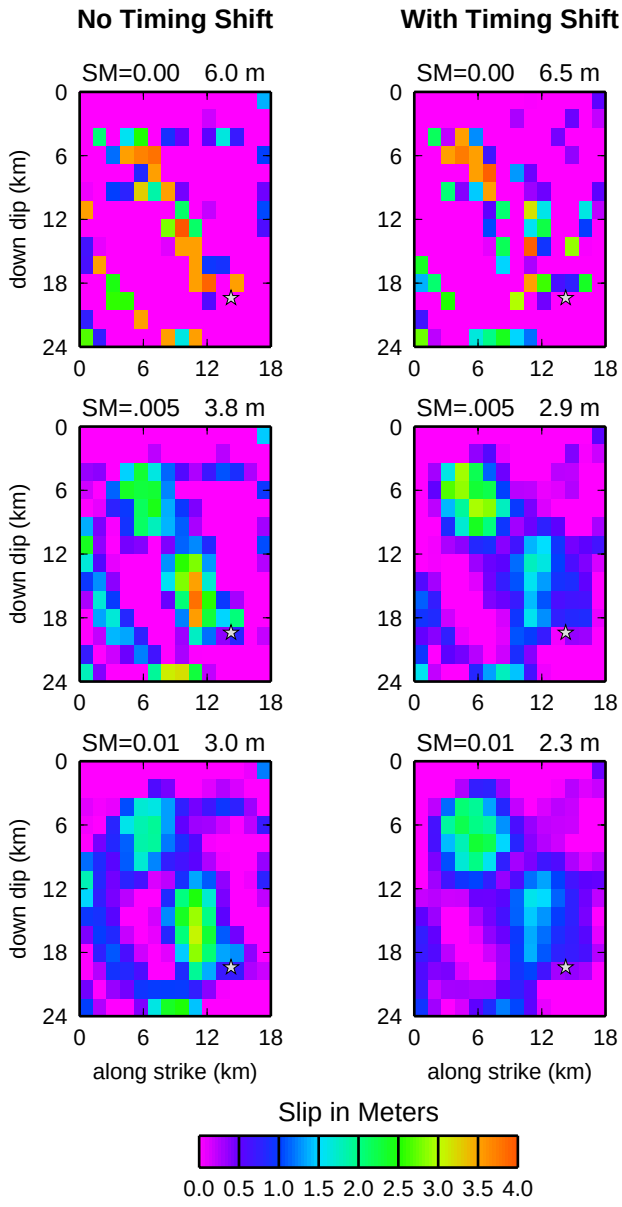

Plate 7: SINGLE column width, COLOR.

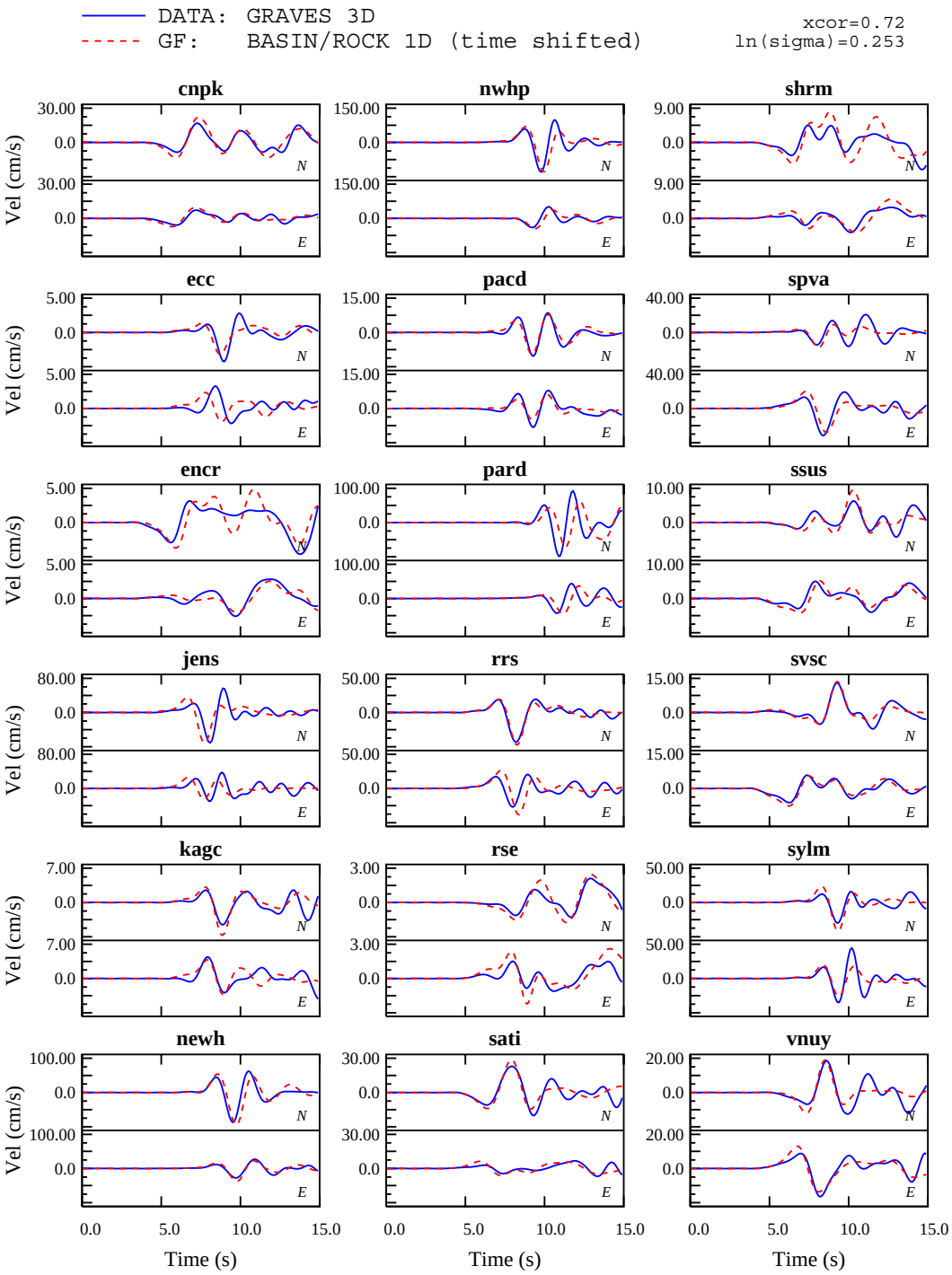

Figure 9: DOUBLE column width, BLACK AND WHITE.